https://doi.org/10.1038/s44306-024-00061-0

THz generation by exchange-coupled spintronic emitters

Roman Adam[1] ✉, Derang Cao[1,2] ✉, Daniel E. Bürgler[1], Sarah Heidtfeld[1,3], Fangzhou Wang[1,3], Christian Greb[1,3], Jing Cheng[4,5], Debamitra Chakraborty[4,5], Ivan Komissarov[5,6], Markus Büscher[1,7], Martin Mikulics[8], Hilde Hardtdegen[8], Roman Sobolewski[5,6] & Claus M. Schneider[1,3]

The mechanism of THz generation in ferromagnet/metal (F/M) bilayers has been typically ascribed to the inverse spin Hall effect (ISHE). Here, we fabricated Pt/Fe/Cr/Fe/Pt multilayers containing two back-to-back spintronic THz emitters separated by a thin ($t_{Cr} \leq$ 3nm) wedge-shaped Cr spacer. In such an arrangement, magnetization alignment of the two Fe films can be controlled by the interplay between Cr-mediated interlayer exchange coupling (IEC) and an external magnetic field. This in turn results in a strong variation of the THz amplitude A, with $A^{\uparrow\downarrow}$ reaching up to 14 times $A^{\uparrow\uparrow}$ (arrows indicate the relative alignment of the magnetization of the two magnetic layers). This observed functionality is ascribed to the interference of THz transients generated by two closely spaced THz emitters. Moreover, the magnetic field dependence $A(H)$ shows a strong asymmetry that points to an additional performance modulation of the THz emitter via IEC and multilayer design.

Terahertz (THz) radiation refers to a part of the electromagnetic spectrum that typically covers frequencies between 300 GHz and 30 THz. Strong interest in developing reliable versatile THz sources stems from the properties of THz radiation that allow unprecedented insight into otherwise inaccessible phenomena in physics[1–9], chemistry[10–13], biology[14–18], astronomy, and materials science[19–21] with a breakthrough potential in a broad range of applications ranging from wireless communication[22–24] to medicine diagnostics[17,18,25]. The full control over the THz generation, detection, polarization state as well as the frequency range is crucial for efficient use of THz radiation in compound-selective chemical imaging, genetic diagnostics or a free-space communication[26,27]. The THz spectral range is particularly attractive for probing interactions in new materials, providing meV and fs resolution in the energy and time space, respectively[28,29]. An overview of physical mechanisms that have been employed for generation of THz transients can be found in[19].

In F/M bilayers superdiffusive spin currents ($\boldsymbol{J}_S$)[30–34] triggered by femtosecond laser pulses in a ferromagnetic layer can be converted into a charge current ($\boldsymbol{J}_C^{ISHE}$) in the adjacent metallic layer by the inverse spin Hall effect (ISHE)[35–37].

The acceleration of electrons forming $\boldsymbol{J}_C^{ISHE}$ generates THz transients that can be either guided along a chip using transmission lines[12,38–40] or propagate into free space[1]. The efficiency of the THz generation is primarily governed by the spin polarization ($\boldsymbol{\sigma}$), which is given by magnetization ($\boldsymbol{M}$), and by the spin Hall angle (θ_{SH}), the value of which is determined by the strength of the spin-orbit coupling (SOC) in the metal layer[1,41–46]. According to[35,47], $\boldsymbol{J}_C^{ISHE}$ is perpendicular to both $\boldsymbol{M}$ and $\boldsymbol{J}_S$, following

$$\boldsymbol{J}_C^{ISHE} = (2\pi/\hbar)\ \theta_{SH}\ (\boldsymbol{J}_S \times \boldsymbol{\sigma}), \tag{1}$$

where $\hbar$ is the Planck constant.

The attractiveness of the optically triggered spintronic emitters stems from a relative simplicity of their design, the tunability of the THz amplitude and polarization, and the compatibility with the standard fabrication technologies. THz radiation has been shown to be easily controllable by a broad range of parameters including magnetic field[1,41–44,48–53], laser fluence[42,42,54], choice of thin-film F and M materials[37], temperature[49,55,56], excitation wavelength[57,58], film thicknesses[42,45,49,50,57,59–61], patterning[62], and light polarization[63].

Several groups worldwide have demonstrated THz emission from more complex layered structures in order to either toggle the spin emitter output between the high- and low-amplitude THz intensity states[64], to increase THz intensity in synthetic antiferromagnets[65,66], or to enhance the overall absorption of the excitation light by covering the emitter with additional dielectric multilayers[58].

[1]Peter Grünberg Institute, Research Centre Jülich, Jülich, Germany. [2]College of Physics, Qingdao University, Qingdao, China. [3]Faculty of Physics, University Duisburg-Essen, Duisburg, Germany. [4]Materials Science Graduate Program, University of Rochester, Rochester, NY, USA. [5]Laboratory for Laser Energetics, University of Rochester, Rochester, NY, USA. [6]Department of Electrical and Computer Engineering, University of Rochester, Rochester, NY, USA. [7]Institut für Laser- und Plasmaphysik, Heinrich-Heine Universität Düsseldorf, Düsseldorf, Germany. [8]Ernst Ruska Centre, Research Centre Jülich, Jülich, Germany. ✉e-mail: r.adam@fz-juelich.de; caodr@qdu.edu.cn

In the present work, we show that THz radiation generated by MgO//Pt/Fe/Cr/Fe/Pt exchange-coupled spintronic (ExCES) emitters can be tuned using interlayer exchange coupling (IEC) and weak magnetic fields. The emitters show the maximum THz output near zero external field and the minimum at saturating magnetic fields. We ascribe the observed functionality to the interference of THz transients generated simultaneously in closely spaced emitters by a single laser pulse.

Results

Exchange-coupled spintronic emitter – principle of operation

The principle of operation of a THz emitter based on the MgO//Pt/Fe/Cr/Fe/Pt multilayers is shown in Fig. 1. Fabrication details are in the Methods. In Fig. 1 we assume that the ISHE mechanism in Pt layers dominates THz generation as reported in, e.g.,[37,45] or[53]. We first neglect THz generation in the Cr layer and assume that the films and interfaces fabricated from the same materials are identical. The arrows and superscripts indicate the directions of $\boldsymbol{M}^{\mathrm{Fe}}$, $\boldsymbol{J}_{\mathrm{S}}^{\mathrm{Fe}}$, and $\boldsymbol{J}_{\mathrm{C}}^{\mathrm{Pt}}$ in the Fe and Pt layers.

The Cr spacer mediates RKKY-type indirect IEC[67] between the two Fe layers, which leads to oscillations between ferro- and antiferromagnetic coupling, depending on the Cr thickness[68]. In zero external magnetic field, this results in either $\boldsymbol{M}^{\uparrow\uparrow}$ or $\boldsymbol{M}^{\uparrow\downarrow}$ relative magnetization alignment in the Fe layers along the Cr wedge. In the $\boldsymbol{M}^{\uparrow\uparrow}$ case [Fig. 1(a)], $\boldsymbol{M}^{\mathrm{Fe1}}$ and $\boldsymbol{M}^{\mathrm{Fe2}}$ point in the same direction. Due to the layer stacking, and following Eq. (1), the currents $\boldsymbol{J}_{\mathrm{S}}^{\mathrm{Pt1}}$, $\boldsymbol{J}_{\mathrm{S}}^{\mathrm{Pt2}}$ (and $\boldsymbol{J}_{\mathrm{C}}^{\mathrm{Pt1}}$, $\boldsymbol{J}_{\mathrm{C}}^{\mathrm{Pt2}}$) point in mutually opposite directions. Resulting THz transients with opposite polarities therefore interfere *destructively*, yielding a minimum THz output.

In contrast, in the $\boldsymbol{M}^{\uparrow\downarrow}$ case [Fig. 1(b)] following the same arguments, transient currents $\boldsymbol{J}_{\mathrm{C}}^{\mathrm{Pt1}}$, $\boldsymbol{J}_{\mathrm{C}}^{\mathrm{Pt2}}$ point in the same direction. In this case, THz transients add *constructively* and generate the resulting THz transient with the maximum amplitude $\boldsymbol{A}_{\max}$.

Figure 2a shows the longitudinal magneto-optic Kerr effect (L-MOKE) signal from an ExCES THz emitter as a function of external field $\mu_0 H$ at one chosen Cr layer thickness t_{Cr} = 1.45 nm (L-MOKE measurement is described in Methods). L-MOKE hysteresis rounding and a reduced remnant magnetization $M_R^{+,-} \approx 0.4 \times \boldsymbol{M}_{sat}$ implies a largely antiparallel $\boldsymbol{M}$ alignment or formation of a multi-domain region within the laser illumination spot. The full set of L-MOKE hystereses for 3 nm > t_{Cr} > 1 nm range is shown in Figure S1. The set illustrates how the varying t_{Cr} affects the shape of magnetic hysteresis and $M_R^{+,-}$.

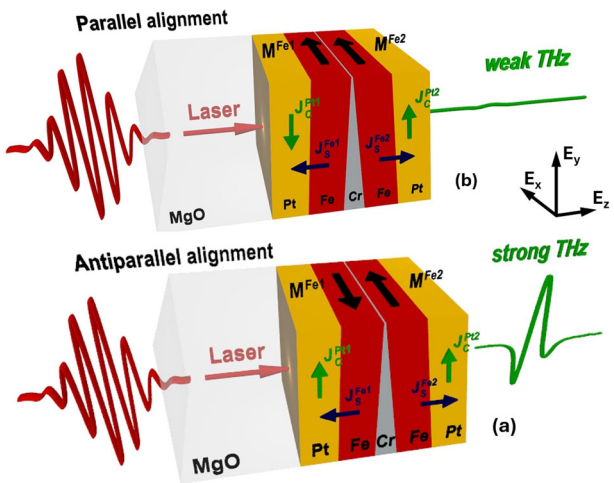

Fig. 1 | Principle of THz emission control in a Pt/Fe/Cr/Fe/Pt multilayer for an antiparallel and parallel alignment of magnetization $\boldsymbol{M}^{\mathrm{Fe1}}$ and $\boldsymbol{M}^{\mathrm{Fe2}}$. The layer sequence consists of two Pt/Fe and Fe/Pt emitters, exchange-coupled by a wedge-shaped Cr spacer and, arranged in a mirror-like geometry with respect to the Cr layer. The thickness t_{Cr} of the Cr spacer varies from 3 to 0 nm. Black arrows mark the magnetization direction of Fe layers $\boldsymbol{M}^{\mathrm{Fe}}$ and the spin currents $\boldsymbol{J}_{\mathrm{S}}$ flowing from Fe to Pt. Green arrows mark the direction of charge currents $\boldsymbol{J}_{\mathrm{C}}$. The parallel (**a**) (antiparallel (**b**)) alignment of $\boldsymbol{J}_{\mathrm{C}}$ results in strong (weak) THz transients due to THz transient superposition. In the figure, ISHE is assumed as a main mechanism and only spin currents flowing from Fe to the neighboring Pt layers are drawn for clarity.

Figure 2b shows THz transients generated by the ExCES emitter at t_{Cr} = 1.45 nm for two magnetic fields $\mu_0 H$ = 8 mT and $\mu_0 H$ = 71 mT. By comparing the transients, it is clear that the *lower* magnetic field results in a significantly *higher* $A_{\max}$. The corresponding FFT power spectra in Fig. 2(c) show no significant differences, both featuring 3- dB cut-off at 1.1 THz and signal extinction at a noise onset at 3.3 THz. The THz measurement schematics is shown in Fig. S2.

An evolution of the peak THz amplitude in a varying magnetic field $A_{\max}(H)$ is displayed in Fig. 2d. It reveals a hysteretic behavior which stands in a stark contrast not only with the L-MOKE loop in Fig. 2a, but also with a typical $A_{\max}(H)$ curve generated by a single-bilayer F/M spintronic emitter[52,53]. In Fig. 2(d), we note that as the magnetic field varies between ± H_{sat}, $A_{\max}(H)$ shows first a minimum, which is subsequently, followed by a sharp enhancement to about 3 × $A_{\max}(H_{\mathrm{sat}})$ near $\mu_0 H \approx +8$ mT. The further increase of the magnetic field leads to an $A_{\max}(H)$ drop, ultimately reaching the minimum at the positive magnetic field saturation. The reverse magnetic field sweep $A_{\max}(H)$ mirrors the one that has just been described. The figure also defines P^+ and P^- as the $A_{\max}(H)$ maxima and the magnetic field tunability range 2 $\mu_0 \Delta H$, the parameters that are described in more detail below.

THz amplitude control via Cr-spacer thickness

Figure 3 illustrates how the $A_{\max}(H)$ varies with t_{Cr}. This is most apparent in the 2.1 nm ≥ t_{Cr} > 0.9 nm range, where $|A_{\max}(H)|$ at t_{Cr} = 1.35 nm shows up to fourteen fold enhancement relative to the $A_{\max}(H_{\mathrm{sat}})$. Nearly all $A_{\max}(H)$ hysteresis curves show P^+ and P^- that also vary with t_{Cr}. Figure 4a shows the evolution of P^+ and P^- along the Cr wedge thickness (full circles and lines). In order to assess the performance of an ExCES THz emitter as an amplifier, we define a figure of merit, FOM = $P^{+,-}/A_{\max}(H_{\mathrm{sat}})$ at each t_{Cr}. Figure 4b shows that the strongest amplification corresponds to FOM ≈ 14 that is reached near $t_{\mathrm{Cr}} \approx 1.2$ nm, suggesting that it corresponds to the near-optimum $M^{\uparrow\downarrow}$ and $M^{\uparrow\uparrow}$ alignment for the current batch of emitters.

Finally, Fig. 4(c) shows 2 $\mu_0 \Delta H$ quantifying the interval of magnetic fields needed to switch the magnetization of the Fe layers from $M^{\uparrow\downarrow}$ to $M^{\uparrow\uparrow}$ configuration. In fact, 2 $\mu_0 \Delta H(t_{\mathrm{Cr}})$ curves, in terms of the shape and peak position, strongly resemble the t_{Cr}-dependence of the IEC constant of similarly fabricated Fe/Cr-wedge/Fe structures presented in Figure 7 of[68]. Direct comparison is shown in Figure S3.

Discussion

In order to understand the generation of the THz transients in ExCES emitters, we calculated the relative alignment of magnetization vectors $\boldsymbol{M}^{\mathrm{Fe1}}$, $\boldsymbol{M}^{\mathrm{Fe2}}$ by numerically solving the equation for the free energy density $E(\theta_1, \theta_2)$ for all possible magnetization angles θ (for a detailed description see Methods). The simulations show that $\boldsymbol{M}^{\mathrm{Fe1}}$ and $\boldsymbol{M}^{\mathrm{Fe2}}$ align co-linearly at ± $\mu_0 \boldsymbol{H}_{\mathrm{sat}}$ and adopt a V-shaped configuration with respect to the magnetic field direction in the $-\mu_0 \boldsymbol{H}_{\mathrm{sat}} < \mu_0 \boldsymbol{H} < +\mu_0 \boldsymbol{H}_{\mathrm{sat}}$ range. Selected snapshots and the evolution of the relative alignment of $\boldsymbol{M}^{\mathrm{Fe1}}$, $\boldsymbol{M}^{\mathrm{Fe2}}$ in the full range of magnetic fields are shown in Figure S4 and the movie in Figure S5. Our simulation also suggests that the antiparallel $\boldsymbol{M}^{\uparrow\downarrow}$ configuration is attained at $\mu_0 \boldsymbol{H}$ = 0 mT, resulting the THz signal maximum P^+ (or P^-). In contrast, in the experiment the maxima are reached near $\mu_0 \boldsymbol{H} \approx \pm 8$ mT [Fig. 4d]. We ascribe this shift to the coercivity and asymmetry in magnetic properties of the two Fe films. This can arise as a consequence of different growth conditions on different substrates for the Fe1 vs. Fe2 and may include differences in the magnetic anisotropy, lattice matching or atomic-level interface smoothness.

The simulations also show that although at $\mu_0 \boldsymbol{H}$ = 0 mT, $\boldsymbol{M}^{\mathrm{Fe1}}$ and $\boldsymbol{M}^{\mathrm{Fe2}}$ are mutually aligned in perfect antiparallel configuration, they are not parallel to $\boldsymbol{H}$ but are tilted by approximately 45 degrees with respect to $\boldsymbol{H}$ direction (Figure S4). This configuration, which is stabilized by the easy axes of the in-plane magnetocrystalline anisotropy, leads to a drop in the measured THz intensity component $E_{\mathrm{y}}^{\mathrm{THz}}$ (perpendicular to $\boldsymbol{H}$) to about 70%

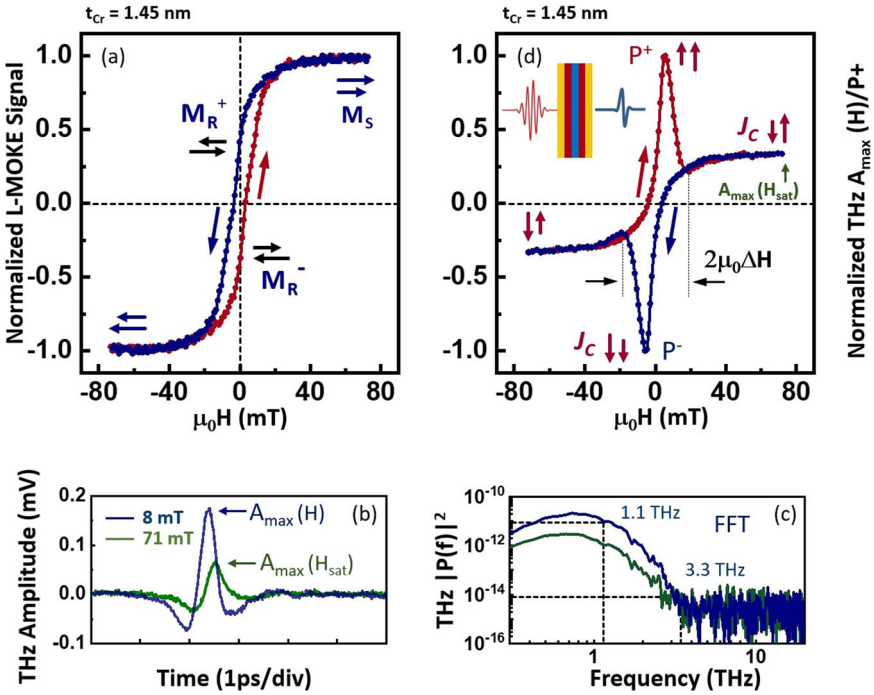

Fig. 2 | Magneto-optic and THz signal from the MgO//Fe/Pt/Cr/Fe/Pt ExCES THz emitter. **a** shows magnetic field dependence of L-MOKE signal at t_{Cr} = 1.45 nm. The hysteresis loop shows reduced remnant magnetizations marked M_R^+ and M_R^- due to antiparallel alignment of the Fe layers' magnetization. The red and blue symbols and the long tilted arrows mark the directions of the magnetic field sweep. **b** THz transients generated by the ExCES THz emitter at $\mu_0 H$ = 8 mT (blue) and $\mu_0 H$ = 71 mT (green). The clearly different maximum amplitudes $A_{max}(H)$ are marked by blue and green arrows. **c** The corresponding FFT power spectra show 3 dB cut-off at 1.1 THz for both magnetic fields. **d** Field dependence of the THz maximum peak amplitude $A_{max}(H)$ generated by the ExCES THz emitter at t_{Cr} = 1.45 nm. Pairs of short red arrows mark the relative J_C^{Pt1} and J_C^{Pt2} alignment that results in weak (antiparallel alignment) and strong (parallel alignment) THz generation. P^+ an P^- denote the peak values of the $A_{max}(H)$ curve for increasing and decreasing field. $A_{max}(H_{sat})$ denotes the THz amplitude in saturation field, i.e., $A_{max}(H_{sat}) = A_{max}(\mu_0 H = 71\ mT)$. The magnetic field tunability range 2 $\mu_0 \Delta H$ is marked by black arrows. The displayed trace shows up to 300% THz signal enhancement at $\mu_0 H = \pm 8$ mT with respect to $A_{max}(H_{sat})$, at this particular t_{Cr}.

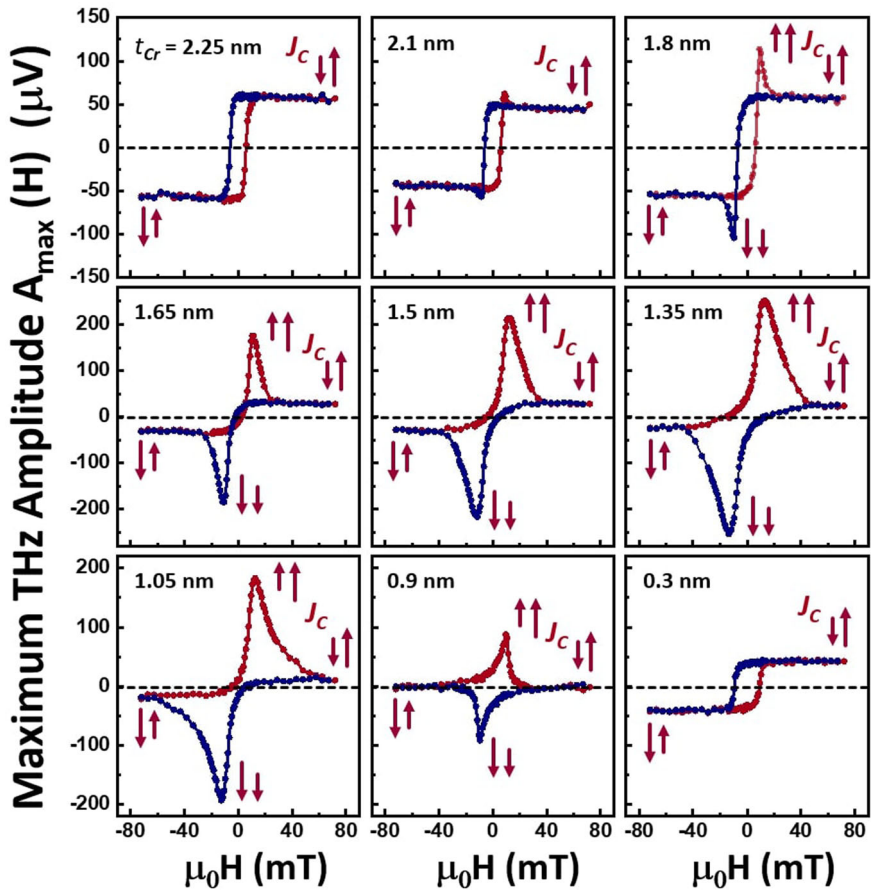

Fig. 3 | Field dependence of the maximum THz amplitude $A_{max}(H)$ at different t_{Cr} (marked at the top left corner of each figure) for the ExCES THz emitter with Cr-wedge in the 3 nm ≥ t_{Cr} > 0 nm range. The joint effect of the external field and IEC leads to an enhancement (suppression) of the THz peak amplitude at Cr thicknesses favoring an antiparallel (parallel) magnetization alignment. The pairs of short red arrows mark the relative alignment of J_C^{Pt1} and J_C^{Pt2}.

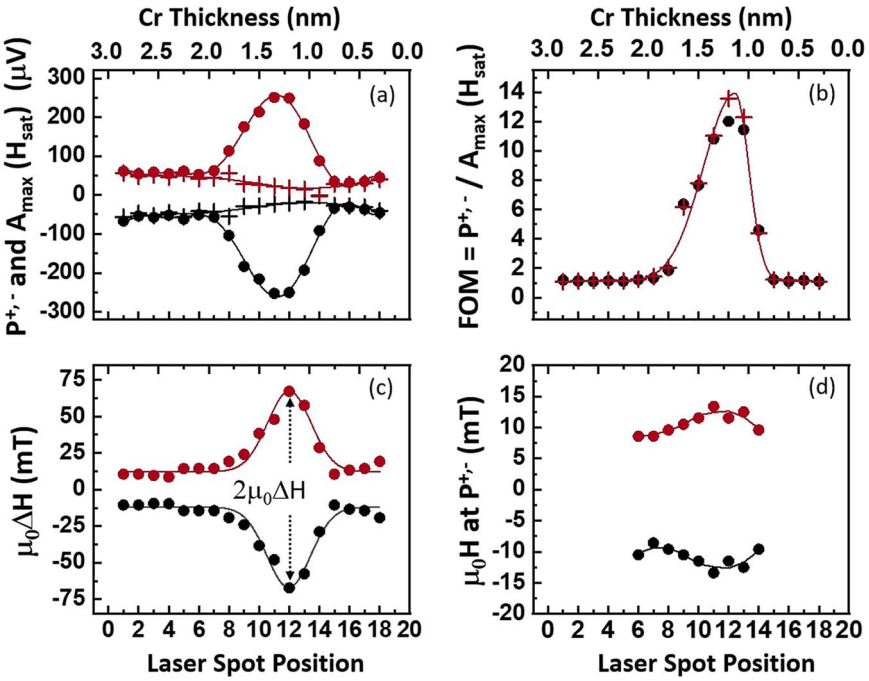

Fig. 4 | Performance parameters for the ExCES THz emitter with Cr-wedge in the 3 nm ≥ t_{Cr} > 0 nm range. a Variation of the peak value of the maximum THz amplitude $A_{max}(H)$, marked $P^{+,-}$ [see Fig. 2d] with t_{Cr} for both increasing (red symbols)- and decreasing magnetic field sweeps (black symbols). A_{max} (H_{sat}) are plotted as red and black crosses. The lines serve as a guides for the eyes. **b** Figure of merit [FOM = $P^{+,-}/A_{max}(H_{sat})$] as a function of t_{Cr} for increasing (red crosses) and decreasing (black dots) field sweeps shows an optimum FOM near t_{Cr} = 1.2 nm. **c** Variation of the field tunability 2 $\mu_0 \Delta H$ with t_{Cr} [for the definition of the field tunability see Fig. 2d]. **d** The magnetic field at which the THz amplitude reaches maximum P^+ (red symbols) or minimum P^- (black symbols) varies with t_{Cr}.

due to the rotation of the THz polarization away from the high sensitivity THz detector-axis (see Methods subsection Experiment:THz measurement). Moreover, due to this tilt, the E_x^{THz} component *parallel* to $\boldsymbol{H}$ can be detected by simply rotating the high-sensitivity axis of the THz detector by 90 degrees, as illustrated in Figure S6. $E_x^{THz} < E_y^{THz}$ suggests that the overall magnetization tilt is either nearly parallel to $\mu_0 \boldsymbol{H}$ or it has a broad asymmetric V-shaped arrangement even at the E_y^{THz} signal maximum.

The performance parameters displayed in Fig. 4a–c show t_{Cr}-dependencies with the maxima centered around t_{Cr} = 1.2 nm, except of $A_{max}(H_{sat})$ which shows a minimum [crosses in Fig. 4 (a)]. We note that while the $A_{max}(H_{sat})$ minimum is reached at the parallel alignment of $\boldsymbol{M}^{Fe1}$, $\boldsymbol{M}^{Fe2}$ enforced by external magnetic fields ± $\mu_0 \boldsymbol{H}_{sat}$, the maxima are due to the antiparallel alignment enforced by IEC near $\mu_0 \boldsymbol{H}$ = 0. The fact that both the maximum and the minimum of $A_{max}(H_{sat})$ occur at the same t_{Cr} indicates optimum- and nearly identical interface properties near $t_{Cr} \approx$ 1.2 nm. The small external field $\mu_0 \boldsymbol{H}$ that is needed to reach the $\boldsymbol{M}^{\uparrow\downarrow}$ or $\boldsymbol{M}^{\downarrow\uparrow}$alignment slightly varies with t_{Cr} as well [Fig. 4(d)] reflecting subtle variations of the energy landscape with t_{Cr}.

Although the performance of ExCES THz emitters is predominantly governed by external magnetic field and by IEC, additional tunability can be achieved by the fabrication process (see Methods). The latter can strongly affect magnetic properties of Fe films as well as transmission, reflection and scattering of $\boldsymbol{J}_S$ and $\boldsymbol{J}_C$ at the F/M interfaces. A close look at the $A_{max}(H)$ dependence reveals that ExCES emitters show only a single THz enhancement during the − $\mu_0 \boldsymbol{H}_{sat}$ to + $\mu_0 \boldsymbol{H}_{sat}$ and + $\mu_0 \boldsymbol{H}_{sat}$ to − $\mu_0 \boldsymbol{H}_{sat}$ sweeps (marked by the red and blue symbols, respectively, in Fig. 3). This is in contrast to a bipolar THz signal enhancement expected for the symmetric IEC supporting two mirrored antiparallel $\boldsymbol{M}^{\uparrow\downarrow}$ alignments at positive and negative field[66]. We therefore simulated the behavior by numerically adding the $A_{max}(H)$ signals of two separate *real* emitters that were fabricated using the exactly same fabrication process as the complete structure of the ExCES emitter. The calculated sum $A_{max}(H)$ qualitatively follows the ExCES emitter performance reproducing the single enhancement per magnetic field sweep (Figure S7). Hence, the unipolar shape of the $A_{max}(H)$ sweeps can be traced back to different coercivity of the Fe layers in *real* emitters, an effect that is not described by the simulations (see Methods).

Relatively recent reports indicate, that a F/M interface can contribute substantially to THz generation even in case of low SOC. The possible mechanisms include the skew scattering[52,69] and the spin-sink effect[70,71]. We consider thermo-electric[30,72–74] and laser-driven demagnetization[36,75–78] effects to be negligible for ExCES emitters due to very thin metallic layers preventing a build-up of thermal gradients and a low excitation power of the laser.

In order to check experimentally the impact of the Fe/Cr interface we fabricated a new Pt(2)/Fe(2) bi-layer and covered one half of it with 3-nm Cr layer. The entire structure was fabricated in-situ and protected by a 3-nm-thick MgO film. Compared to the Fe/Pt - side, the Pt/Fe/**Cr** side reveals an overall *drop* of $A_{max}(H)$ by about 30%. In the ISHE picture, the THz amplitudes from Pt/Fe and Fe/Cr emitters *add* due to the opposite sign of θ_{SH}. The observed drop suggests the presence of additional mechanisms. Following the laser excitation, a fraction of $\boldsymbol{J}_S$ in the Pt/Fe/**Cr** structure superdiffuses into Cr, in contrast to Pt/Fe/MgO, where the entire $\boldsymbol{J}_S$ enters the Pt layer. The fraction of $\boldsymbol{J}_S$ that passes through the Fe/Cr interface can generate a THz transient with the opposite polarity via skew scattering[52,69]. In addition, the Cr-induced spin-sink effect earlier described in[70] and[71] can reduce $\boldsymbol{J}_S$ in Pt resulting in a further overall drop of the THz amplitude.

In conclusion, our measurements show that controlling the magnetic configurations in our ExCES emitters permits convenient tunability of the THz radiation amplitude and polarization via IEC and weak external fields. Compared to simpler spintronic THz emitters based on soft ferromagnet/heavy metal bi-layers, ExCES THz emitters show a complementary behavior of $A_{max}(H)$, i.e., they demonstrate low THz amplitude at large magnetic fields $\mu_0 H \rightarrow \mu_0 H_{sat}$ and the THz maximum near $\mu_0 H$ = 0 mT. In addition, our ExCES emitters show up-to 14-fold enhancement of the THz amplitude $A_{max}(H)/ A_{max}(H_{sat})$ for the $M^{\uparrow\downarrow}$ vs the $M^{\uparrow\uparrow}$ configurations. We ascribe this additional flexibility in ExCES emitters to a controlled constructive or destructive interference of THz transients, generated by the two closely spaced inversely stacked F/M bilayers. The switching complementarity, together with the two-input control (M^{FM1} and M^{FM2}) show a potential for logic operations in THz frequency range.

The straightforward control of the relative alignment of $\boldsymbol{M}^{Fe1}$, $\boldsymbol{M}^{Fe2}$ by IEC and $\boldsymbol{H}$, results in a good control of the THz polarity and linear polarization direction. ExCES emitters show also a strong potential for the generation of elliptically-polarized THz and possibly beam steering using phase control of the two THz emitters[79]. This can be possibly achieved by introducing a capping and a spacer material with fitting refractive index in THz range.

Apart from a few potentially practical outcomes, our investigation of THz radiation from the ExCES THz emitters provides an insight into the spin transport in layered thin-film structures beyond the magneto-optical measurements. Our study identified the degree of magnetization alignment, symmetry of ICE and interface quality, the spin-sink effect as the major important factors affecting the overall performance. Demagnetization and thermal gradients, on the other hand, do not seem to play a significant role, due to the use of low laser fluence in our experiments and ultra-thin metallic films the with low thermo-electric constant. In the ExCES THz emitters, we employed a Cr metallic spacers because of the excellent Fe/Cr lattice matching, the proven MBE deposition technology and the well-described magnetization control by IEC. On the other hand, the magnetization is controlled via conducting electrons in Cr. Therefore, laser-generated spin currents are not blocked what leads to the spin sink effect, skew scattering and possibly cross-talk effect. Replacement by a suitable insulating spacer has a potential of a further enhancement of the overall performance. Some investigation may be needed to find the fabrication parameters for atomically smooth layers and high quality interfaces.

The prospect of THz generation and the resistivity tuning over few orders of magnitude using multilayer structures points to a possible merge of the low-power spintronics circuitry with the high-frequency THz emitters.

Methods

Fabrication

We used molecular-beam epitaxy (MBE) at the base pressure of about 2×10^{-10} mbar for the deposition of MgO (substrate) //Pt(2)/Fe(2)/Cr-wedge/Fe(2)/Pt(2) multilayers and MgO (substrate) //Pt(2)/Fe(2)/Cr(3) on top of optically polished 10×10 mm^2 MgO substrates with (100) surface orientation. The numbers in parenthesis next to the elements mark the respective layer thickness in nanometers. During the deposition, the thickness of each layer was monitored by a quartz crystal microbalance. The thickness of the Cr-wedge varied from 3 to 0 nm over a lateral length of about 8 mm, forming a Cr-wedge with a slope of 0.4 μrad. The thickness of all other layers was kept constant. For the purpose of clarity in the discussion and figure descriptions, we mark the layers closer to (further from) the substrate as Pt1 and Fe1 (Pt2 and Fe2) in the sequence of deposition throughout the manuscript.

Experiment: L-MOKE measurement

The IEC strength in M/F/spacer wedge/F/M multilayers varies with spacer thickness along the wedge. We recorded the position-dependent in-plane magnetization of the multilayer stack using the longitudinal magneto-optic Kerr effect (L-MOKE geometry) by scanning the laser spot position along the Cr thickness gradient. For the L-MOKE measurements, we employ a cw laser diode laser chopped at 238 Hz and incident to the surface at an angle of 60°. The beam reflected from the sample surface was then detected by a balanced photo-diode pair and recorded by a lock-in amplifier. The laser spot at the sample surface was slightly elongated due to the oblique incidence. The long axis of the elliptical laser-spot was aligned along the constant Cr thickness. The minor axis of the elliptical laser spot (≈ 100 µm), due to the very small incline of the Cr wedge, covered only a negligible range of its thickness (< 0.04 nm). In the range 3 nm > t_{Cr} > 2 nm, the $M(H)$ loops display a high squareness with a coercive field $\mu_0 H_C \approx 10$ mT, reflecting a parallel alignment- and FM coupling between Fe layers. In this Cr thickness range, both Fe layer magnetizations reverse synchronously during magnetic field sweep, resulting in a sharp transition from $\boldsymbol{M}^{\uparrow\uparrow}$ to $\boldsymbol{M}^{\downarrow\downarrow}$ and vice versa. For smaller (2 nm > t_{Cr} > 1 nm) Cr thicknesses the L-MOKE hysteresis curves show significant rounding and lower remnant magnetization, pointing to a deviation from the strictly parallel alignment of layer magnetizations. The hysteresis captures the magneto-optic signal proportional to the projection of the overall in-plane magnetization $\boldsymbol{M} = \boldsymbol{M}^{Fe1} + \boldsymbol{M}^{Fe2}$ to the external $\boldsymbol{H}$ direction. Throughout the manuscript, red and blue symbols indicate the directions of magnetic field sweeps. For smooth interfaces, the Cr-spacer-mediated IEC results in either ferromagnetic, antiferromagnetic (bilinear) or 90° (biquadratic) coupling between $\boldsymbol{M}^{Fe1}$ and $\boldsymbol{M}^{Fe2}$ [68,80–87] and the IEC strength has been demonstrated to show oscillatory behavior up to 3 nm of Cr spacer[68].

Experiment: THz measurement

The experimental THz setup is schematically shown in Supplementary Fig. S2. We recorded THz transients at a chosen magnetic field H and Cr spacer thickness t_{Cr}. From the set of THz transients we extracted the maximum THz amplitudes $A_{max}(H, t_{Cr})$ as a function of $\mu_0 H$ and t_{Cr}. We first positioned the ExCES THz emitter at the laser beam focus in perpendicular incidence geometry with the beam impinging at the multilayer surface at the thickest part of the Cr wedge (at about 2 mm distance from the perfectly aligned substrate edge). The laser fluence was kept at 6.5 μJ/cm^2 during all measurements. By varying the time delay between the incident pulse train and the pulses triggering the photoconducting THz detector, we recorded THz transients at a chosen set of static magnetic fields $\mu_0 H$. For the next set of THz transients at the next chosen Cr thicknesses, we shifted the laser spot position along the incline of the Cr wedge by moving the sample by 400 to 800 μm steps, depending on targeted spacer thickness. Note, that the THz photoconductive detector detects the THz polarization component aligned between the vertices of the triangular metallic notches of the detector[88,89] and is blind to the THz polarization aligned perpendicular to the triangular vertices. After recording the full set of THz transients, we first extracted the *maximum amplitude* A_{max} of each recorded THz transient and then plotted the magnetic hysteresis loop $A_{max}(H)$ for each spacer thickness[90]. The latter data set allows analysis of the $A_{max}(H)$ variation due to varying IEC along the wedge-shaped Cr spacer.

Simulation

We calculated relative alignment of $\boldsymbol{M}^{Fe1}$ and $\boldsymbol{M}^{Fe2}$ by first calculating the free energy density E:

$\boldsymbol{E}(\theta_1, \theta_2) =$	$-HM_S[\, d_1 \cos(\theta_1) + d_2 \cos(\theta_2)]$	Zeeman energy
	$+\frac{1}{4}[K_1\, d_1 \cos^2(2\,\theta_1) + K_2\, d_2 \cos^2(2\,\theta_2)]$	Magnetocrystalline anisotropy
	$-J_1 \cos(\theta_1 - \theta_2)$	Bilinear coupling
	$-J_2 \cos^2(\theta_1 - \theta_2)$	Biquadratic coupling

taking into account the Zeeman energy, the in-plane magnetocrystalline anisotropies of the two Fe layers K_1, K_2, the bilinear (J_1) and biquadratic (J_2) coupling terms and the angles between $\boldsymbol{M}^{Fe1}$, $\boldsymbol{M}^{Fe2}$ and the $\boldsymbol{H}$ direction, θ_1 and θ_2, respectively. H is the external field intensity, M_S saturation magnetization, d_1, d_2 thicknesses of ferromagnetic layers ($d_1 = d_2$ for our multilayer)[67]. In the second step, we found magnetization alignment angles θ_1 and θ_2, by finding the $E(\theta_1, \theta_2)$ minimum for every external magnetic field. In our experiments, the easy axes of the fourfold magnetic anisotropy are at an angle of 45 degrees to the direction of the applied magnetic field.

Data availability

Data sets generated during the current study are available from the corresponding author on reasonable request.

Received: 6 September 2024; Accepted: 15 October 2024;
Published online: 29 November 2024

References

1. Kampfrath, T., Tanaka, K. & Nelson, K. A. Resonant and nonresonant control over matter and light by intense terahertz transients. *Nat. Photon.* **7**, 680–690 (2013).

2. Nanni, E. A. et al. Terahertz-driven linear electron acceleration. *Nat. Commun.* **6**, 8486 (2015).
3. Jia, M. et al. Efficient manipulations of circularly polarized terahertz waves with transmissive metasurfaces. *Light Sci. Appl.* **8**, 16 (2019).
4. Zhou, C. et al. Broadband terahertz generation via the interface inverse Rashba-Edelstein effect. *Phys. Rev. Lett.* **121**, 086801 (2018).
5. Feng, Z. et al. Spintronic terahertz emitter. *J. Appl. Phys.* **129**, 010901 (2021).
6. Jepsen, P., Cooke, D. & Koch, M. Terahertz spectroscopy and imaging – modern techniques and applications. *Laser Photon. Rev.* **5**, 124–166 (2011).
7. Papaioannou, E. T. & Beigang, R. THz spintronic emitters: a review on achievements and future challenges. *Nanophotonics* **10**, 1243–1257 (2021).
8. Wu, W., Yaw Ameyaw, C., Doty, M. F. & Jungfleisch, M. B. Principles of spintronic THz emitters. *J. Appl. Phys.* **130**, 091101 (2021).
9. Kida, N., Miyamoto, T. & Okamoto, H. Emission of terahertz electromagnetic waves: A new spectroscopic method to investigate physical properties of solids. *J. Phys. Soc. Jpn* **91**, 112001 (2022).
10. Ajito, K. & Ueno, Y. THz chemical imaging for biological applications. *IEEE Trans. THz Sci. Technol.* **1**, 293–300 (2011).
11. Zeitler, J. A. et al. Terahertz pulsed spectroscopy and imaging in the pharmaceutical setting - a review. *J. Pharm. Pharmacol.* **59**, 209–223 (2010).
12. Serita, K., Kobatake, S. & Tonouchi, M. I-design terahertz microfluidic chip for attomole-level sensing. *J. Phys. Photon.* **4**, 034005 (2022).
13. Milot, R. L. et al. Charge-carrier dynamics in 2d hybrid metal–halide perovskites. *Nano Lett.* **16**, 7001–7007 (2016).
14. Fitzgerald, A. J. et al. An introduction to medical imaging with coherent terahertz frequency radiation. *Phys. Med. Biol.* **47**, R67 (2002).
15. Yang, X. et al. Biomedical applications of terahertz spectroscopy and imaging. *Trends Biotechnol.* **34**, 810–824 (2016).
16. Pickwell, E. & Wallace, V. P. Biomedical applications of terahertz technology. *J. Phys. D Appl. Phys.* **39**, R301 (2006).
17. Choi, W. J. et al. Chiral phonons in microcrystals and nanofibrils of biomolecules. *Nat. Photon.* **16**, 366–373 (2022).
18. Chakraborty, D. et al. Development of terahertz imaging markers for pancreatic ductal adenocarcinoma using maximum a posteriori probability (map) estimation. *ACS Omega* **8**, 9925–9933 (2023).
19. Lewis, R. Materials for terahertz engineering. In *Springer Handbook of Electronic and Photonic Materials* (eds Kasap, S. & Capper, P.), p. 1–1 (Springer International Publishing, Cham, 2017).
20. Ferguson, B. & Zhang, X.-C. Materials for terahertz science and technology. *Nat. Mater.* **1**, 26–33 (2002).
21. Shi, J. et al. THz photonics in two dimensional materials and metamaterials: properties, devices and prospects. *J. Mater. Chem. C* **6**, 1291–1306 (2018).
22. Seeds, A. J., Shams, H., Fice, M. J. & Renaud, C. C. Terahertz photonics for wireless communications. *J. Lightwave Technol.* **33**, 579–587 (2015).
23. Tataria, H. et al. 6g wireless systems: vision, requirements, challenges, insights, and opportunities. *Proc. IEEE* **109**, 1166–1199 (2021).
24. Nagatsuma, T., Ducournau, G. & Renaud, C. C. Advances in terahertz communications accelerated by photonics. *Nat. Photon.* **10**, 371–379 (2016).
25. Peng, Y., Shi, C., Wu, X., Zhu, Y. & Zhuang, S. Terahertz imaging and spectroscopy in cancer diagnostics: a technical review. *BME Front.* https://spj.science.org/doi/abs/10.34133/2020/2547609 (2020).
26. Tonouchi, M. Cutting-edge terahertz technology. *Nat. Photon.* **1**, 97–105 (2007).
27. Dhillon, S. S. et al. The 2017 terahertz science and technology roadmap. *J. Phys. D Appl. Phys.* **50**, 043001 (2017).
28. Neu, J. & Schmuttenmaer, C. Tutorial: an introduction to terahertz time domain spectroscopy (THz -TDS). *J. Appl. Phys.* **124**, 231101 (2018).
29. Baierl, S. et al. Nonlinear spin control by terahertz-driven anisotropy fields. *Nat. Photon.* **10**, 715–718 (2016).
30. Uchida, K. et al. Observation of the spin Seebeck effect. *Nature* **455**, 778–781 (2008).
31. Battiato, M., Carva, K. & Oppeneer, P. M. Superdiffusive spin transport as a mechanism of ultrafast demagnetization. *Phys. Rev. Lett.* **105**, 027203 (2010).
32. Battiato, M., Carva, K. & Oppeneer, P. M. Theory of laser-induced ultrafast superdiffusive spin transport in layered heterostructures. *Phys. Rev. B* **86**, 024404 (2012).
33. Bauer, G. E. W., Saitoh, E. & van Wees, B. J. Spin caloritronics. *Nat. Mater.* **11**, 391–399 (2012).
34. Nenno, D. M., Binder, R. & Schneider, H. C. Simulation of hot-carrier dynamics and terahertz emission in laser-excited metallic bilayers. *Phys. Rev. Appl.* **11**, 054083 (2019).
35. Saitoh, E., Ueda, M., Miyajima, H. & Tatara, G. Conversion of spin current into charge current at room temperature: Inverse spin-Hall effect. *Appl. Phys. Lett.* **88**, 182509 (2006).
36. Lu, W.-T., Zhao, Y., Battiato, M., Wu, Y. & Yuan, Z. Interface reflectivity of a superdiffusive spin current in ultrafast demagnetization and terahertz emission. *Phys. Rev. B* **101**, 014435 (2020).
37. Cheng, J. et al. Terahertz inverse spin Hall effect in spintronic nanostructures with various ferromagnetic materials. *J. Magn. Magn. Mater.* **593**, 171641 (2024).
38. Smith, L., Gomma, W., Esmaeilsabzali, H. & Darcie, T. Tapered transmission lines for terahertz systems. *Opt. Express* **29**, 17295–17303 (2021).
39. Smith, P., Auston, D. & Nuss, M. Subpicosecond photoconducting dipole antennas. *IEEE J. Quant. Electron.* **24**, 255–260 (1988).
40. Singh, P. K. & Sonkusale, S. High speed terahertz modulator on the chip based on tunable terahertz slot waveguide. *Sci. Rep.* **7**, 40933 (2017).
41. Kampfrath, T. et al. Terahertz spin current pulses controlled by magnetic heterostructures. *Nat. Nanotechnol.* **8**, 256–260 (2013).
42. Seifert, T. et al. Efficient metallic spintronic emitters of ultrabroadband terahertz radiation. *Nat. Photon.* **10**, 483–488 (2016).
43. Feng, Z. et al. Highly efficient spintronic terahertz emitter enabled by metal–dielectric photonic crystal. *Adv. Opt. Mater.* **6**, 1800965 (2018).
44. Seifert, T. et al. Ultrabroadband single-cycle terahertz pulses with peak fields of 300 kV cm^{-1} from a metallic spintronic emitter. *Appl. Phys. Lett.* **110**, 252402 (2017).
45. Torosyan, G., Keller, S., Scheuer, L., Beigang, R. & Papaioannou, E. T. Optimized spintronic terahertz emitters based on epitaxial grown fe/pt layer structures. *Sci. Rep.* **8**, 1311 (2018).
46. Walowski, J. & Münzenberg, M. Perspective: ultrafast magnetism and thz spintronics. *J. Appl. Phys.* **120**, 140901 (2016).
47. Kimura, T., Otani, Y., Sato, T., Takahashi, S. & Maekawa, S. Room-temperature reversible spin hall effect. *Phys. Rev. Lett.* **98**, 156601 (2007).
48. Seifert, T. et al. Terahertz spin currents and inverse spin hall effect in thin-film heterostructures containing complex magnetic compounds. *SPIN* **07**, 1740010 (2017).
49. Huisman, T. J. et al. Spin-photo-currents generated by femtosecond laser pulses in a ferrimagnetic GdFeCo/Pt bilayer. *Appl. Phys. Lett.* **110**, 072402 (2017).
50. Chen, M., Mishra, R., Wu, Y., Lee, K. & Yang, H. Terahertz emission from compensated magnetic heterostructures. *Adv. Opt. Mater.* **6**, 1800430 (2018).
51. Hibberd, M. T. et al. Magnetic-field tailoring of the terahertz polarization emitted from a spintronic source. *Appl. Phys. Lett.* **114**, 031101 (2019).
52. Heidtfeld, S. et al. Generation of terahertz transients from $Co_2Fe_{0.4}Mn_{0.6}$ Si-Heusler-alloy/normal-metal nanobilayers excited by femtosecond optical pulses. *Phys. Rev. Res.* **3**, 043025 (2021).
53. Adam, R. et al. Magnetically and optically tunable terahertz radiation from ta/nife/pt spintronic nanolayers generated by femtosecond laser pulses. *Appl. Phys. Lett.* **114**, 212405 (2019).

54. Zhang, Q. et al. Terahertz emission from anomalous hall effect in a single-layer ferromagnet. *Phys. Rev. Appl.* **12**, 054027 (2019).
55. Matthiesen, M. et al. Temperature dependent inverse spin Hall effect in Co/Pt spintronic emitters. *Appl. Phys. Lett.* **116**, 212405 (2020).
56. Kholid, F. N. et al. Temperature dependence of the picosecond spin Seebeck effect. *Appl. Phys. Lett.* **119**, 032401 (2021).
57. Papaioannou, E. T. et al. Efficient terahertz generation using Fe/Pt spintronic emitters pumped at different wavelengths. *IEEE Trans. Magn.* **54**, 1–5 (2018).
58. Herapath, R. I. et al. Impact of pump wavelength on terahertz emission of a cavity-enhanced spintronic trilayer. *Appl. Phys. Lett.* **114**, 041107 (2019).
59. Cheng, L. et al. Far out-of-equilibrium spin populations trigger giant spin injection into atomically thin MoS_2. *Nat. Phys.* **15**, 347–351 (2019).
60. Zhang, Q. et al. Terahertz emission from CoFeB/Cr/Pt trilayers: the role of Cr as both a spin current transporter and generator. *Appl. Phys. Lett.* **118**, 232401 (2021).
61. Schneider, R. et al. Spintronic GdFe/Pt THz emitters. *Appl. Phys. Lett.* **115**, 152401 (2019).
62. Yang, D. et al. Powerful and tunable THz emitters based on the Fe/Pt magnetic heterostructure. *Adv. Opt. Mater.* **4**, 1944–1949 (2016).
63. Huisman, T. J. et al. Femtosecond control of electric currents in metallic ferromagnetic heterostructures. *Nat. Nanotechnol.* **11**, 455–458 (2016).
64. Fix, M., Schneider, R., Michaelis de Vasconcellos, S., Bratschitsch, R. & Albrecht, M. Spin valves as magnetically switchable spintronic THz emitters. *Appl. Phys. Lett.* **117**, 132407 (2020).
65. Zhang, Q. et al. Terahertz emission from an exchange-coupled synthetic antiferromagnet. *Phys. Rev. Appl.* **13**, 054016 (2020).
66. Ogasawara, Y. et al. Laser-induced terahertz emission from layered synthetic magnets. *Appl. Phys. Express* **13**, 063001 (2020).
67. Bürgler, D. E., Grünberg, P., Demokritov, S. O. & Johnson, M. T. *Handbook of Magnetic Materials*, vol. 13, p. 1–85 (Elsevier, 2001).
68. Schmidt, C. M., Bürgler, D. E., Schaller, D. M., Meisinger, F. & Güntherodt, H.-J. Correlation of short-period oscillatory exchange coupling to nanometer-scale lateral interface structure in Fe/Cr/Fe(001). *Phys. Rev. B* **60**, 4158–4169 (1999).
69. Gueckstock, O. et al. Terahertz spin-to-charge conversion by interfacial skew scattering in metallic bilayers. *Adv. Mater.* **33**, 2006281 (2021).
70. Tserkovnyak, Y., Brataas, A., Bauer, G. E. W. & Halperin, B. I. Nonlocal magnetization dynamics in ferromagnetic heterostructures. *Rev. Mod. Phys.* **77**, 1375–1421 (2005).
71. Harii, K. et al. Spin pumping in a ferromagnetic/nonmagnetic/spin-sink trilayer film: spin current termination. *Key Eng. Mater.* **508**, 5 (2012).
72. Adachi, H., ichi Uchida, K., Saitoh, E. & Maekawa, S. Theory of the spin Seebeck effect. *Rep. Prog. Phys.* **76**, 036501 (2013).
73. Feng, Z. et al. Anomalous Nernst effect induced terahertz emission in a single ferromagnetic film. *Nano Lett.* **23**, 8171–8179 (2023).
74. Chen, Y.-J. & Huang, S.-Y. Light-induced thermal spin current. *Phys. Rev. B* **99**, 094426 (2019).
75. Zhang, W. et al. Ultrafast terahertz magnetometry. *Nat. Commun.* **11**, 4247 (2020).
76. Huang, L. et al. Direct observation of terahertz emission from ultrafast spin dynamics in thick ferromagnetic films. *Appl. Phys. Lett.* **115**, 142404 (2019).
77. Huisman, T. J., Mikhaylovskiy, R. V., Tsukamoto, A., Rasing, T. & Kimel, A. V. Simultaneous measurements of terahertz emission and magneto-optical Kerr effect for resolving ultrafast laser-induced demagnetization dynamics. *Phys. Rev. B* **92**, 104419 (2015).
78. Chekhov, A. L. et al. Ultrafast demagnetization of iron induced by optical versus terahertz pulses. *Phys. Rev. X* **11**, 041055 (2021).
79. Zeng, H. et al. A review of terahertz phase modulation from free space to guided wave integrated devices. *Nanophotonics* **11**, 415–437 (2022).
80. Grünberg, P., Schreiber, R., Pang, Y., Brodsky, M. B. & Sowers, H. Layered magnetic structures: Evidence for antiferromagnetic coupling of Fe layers across Cr interlayers. *Phys. Rev. Lett.* **57**, 2442–2445 (1986).
81. Rührig, M. et al. Domain observations on Fe-Cr-Fe layered structures – evidence for a biquadratic coupling effect. *Phys. Stat. Sol. (a)* **125**, 635–656 (1991).
82. Parkin, S. S. P. Systematic variation of the strength and oscillation period of indirect magnetic exchange coupling through the 3d, 4d, and 5d transition metals. *Phys. Rev. Lett.* **67**, 3598–3601 (1991).
83. Pierce, D. T., Stroscio, J. A., Unguris, J. & Celotta, R. J. Influence of Cr growth on exchange coupling in Fe/Cr/Fe(100). *Phys. Rev. B* **49**, 14564–14572 (1994).
84. Bruno, P. Theory of interlayer magnetic coupling. *Phys. Rev. B* **52**, 411–439 (1995).
85. Stiles, M. D. Interlayer exchange coupling. *J. Magn. Magn. Mater.* **200**, 322–337 (1999).
86. Parkin, S. S. P., More, N. & Roche, K. P. Oscillations in exchange coupling and magnetoresistance in metallic superlattice structures: Co/Ru, Co/Cr, and Fe/Cr. *Phys. Rev. Lett.* **64**, 2304–2307 (1990).
87. Stiles, M. *Interlayer Exchange Coupling*. 200 (Ultrathin Magnetic Structures III, Springer-Verlag, 2004).
88. Chen, G. et al. Transient THz emission and effective mass determination in highly resistive gaas crystals excited by femtosecond optical pulses. *Crystals* **12**, 1635 (2022).
89. Geižutis, A. et al. Terahertz radiation emitters and detectors. *Opt. Mater.* **30**, 786–788 (2008).
90. Büscher, M. et al. JuSPARC—the Jülich short-pulsed particle and radiation center. *J. Large Scale Res. Fac.* **6**, A138 (2020).

Acknowledgements

The work at the Research Centre Jülich (FZJ) was performed within the JuSPARC strategy project funded by the BMBF. The research at the University of Rochester was supported in part by the University of Rochester Awards Program and the DOE Grant DE-SC0022473. Authors thank Thomas Jansen for the MBE deposition of the multilayers.

Author contributions

R.A. initiated the project and designed the structures. D.C., S.H., and R.A. carried out the THz experiments. D.C. carried out the L-MOKE experiments. D.E.B. designed the fabrication process and fabricated the samples. S.H., F.W., C.G., and J.C. set up the experiment and discussed the results. R.A. and D.C. analyzed the data and wrote the manuscript. D.E.B performed the simulations of the free energy density. I.K., J.C., D. Ch., R.S. M.B., M.M., and H.H. contributed to the discussion of results and the manuscript writing and revisions. R.S., C.M.S., and R.A. coordinated the project and the work on the manuscript's final version. All co-authors contributed to the data interpretation, internal discussion, and the manuscript text.

Funding

Open Access funding enabled and organized by Projekt DEAL.

Competing interests

The authors declare no competing interests.

Additional information

Supplementary information The online version contains supplementary material available at https://doi.org/10.1038/s44306-024-00061-0.

Correspondence and requests for materials should be addressed to Roman Adam or Derang Cao.